arXiv:1404.7312v1 [hep-ph] 29 Apr 2014

Spectral Functions from the Functional Renormalization Group

Jochen Wambach[a,b,*], Ralf-Arno Tripolt[a], Nils Strodthoff[c], Lorenz von Smekal[a,d]

[a] *Institut für Kernphysik - Theoriezentrum, Technische Universität Darmstadt, Germany*
[b] *GSI Helmholtzzentrum für Schwerionenforschung GmbH, Germany*
[c] *Institut für Theoretische Physik, Ruprecht-Karls-Universität Heidelberg, Germany*
[d] *Institut für Theoretische Physik, Justus-Liebig-Universität Giessen, Germany*

Abstract

In this article we wish to present a new method to obtain spectral functions at finite temperature and density from the Functional Renormalization Group (FRG). The FRG offers a powerful non-perturbative tool to deal with phase transitions in strong-interaction matter under extreme conditions and their fluctuation properties. Based on a thermodynamically consistent truncation we derive flow equations for pertinent two-point functions in Minkowski space-time. We demonstrate the feasibility of the method by calculating mesonic spectral functions in hot and dense hadronic matter using the quark-meson model as a simple example.

Keywords: spectral function, analytic continuation, QCD phase diagram

1. Introduction

The in-medium modifications of hadron properties have been dear to Gerry's heart and his work on this subject has made him and his collaborators major drivers of this field for several decades [1, 2]. The discussions are far from over and we wish to pay tribute to Gerry's physical insights by adding a new and promising alternative for computing real-time spectral functions in hot and

*Corresponding author.
Talk presented at "45 years of nuclear theory at Stony Brook - A tribute to Gerald E. Brown".
Email address: Jochen.Wambach@physik.tu-darmstadt.de (Jochen Wambach)

dense QCD matter. The aim is to set up a framework that goes beyond mean-field theory (which Gerry employed very successfully during his career) by incorporating quantum fluctuations. This is particularly important for the understanding of the restoration of broken chiral symmetry in the hadronic medium.

Spectral functions encode information on the particle spectrum as well as collective excitations of a given system. A thermodynamically consistent calculation beyond the Hartree-Fock level of such real-time observables represents an inherently difficult problem. Although mean-field calculations might capture the gross features of the equilibrium properties, quantitative predictions and correct descriptions of critical phenomena require the proper inclusion of fluctuations. Several self-consistent methods are available among which the Functional Renormalization Group (FRG) is particularly suitable and widely used in quantum field theory and condensed matter physics [3, 4, 5, 6, 7, 8, 9].

A technical difficulty which is common to all Euclidean approaches to Quantum Field Theory is the need to analytically continue from imaginary to real time especially for dynamic processes with time-like momentum transfers. At finite temperature these continuations are often based on numerical (i.e. noisy) data at discrete Matsubara frequencies and several approximate methods for the reconstruction of real-time spectral functions have been used [10, 11, 12, 13] with varied success. Therefore any approach that can deal with the analytic continuation explicitly is highly desirable. Such alternative approaches have been proposed in [14, 15] and [16]. They involve an analytic continuation on the level of the FRG flow equations for two-point correlation functions and have been applied in [15] to a model system with O(4) internal symmetry in vacuum. More recently, this method has been applied to obtain spectral functions from the quark-meson model at finite temperature and density [17]. These studies form the basis for the present discussion of hadronic matter at high temperatures and large baryo-chemical potentials.

2. The Functional Renormalization Group

To set the stage we start out with the basic ideas of the FRG, by discussing the effective potential of a system in thermal equilibrium, the ensuing correlation functions and their flow equations.

2.1. Effective action

The principal object of statistical physics is the (Euclidean) partition function Z from which the equilibrium properties of a thermal system can be derived. Z can be represented as a Feynman path integral (for simplicity in a real field variable ϕ). In the presence of an external source j it reads:

$$Z[j] = e^{W[j]} = \int [\mathcal{D}\phi] \; e^{-S[\phi] + \int d^4x \; \phi(x) j(x)} \; , \tag{1}$$

and $W[j]$ generates all n-point Green functions via functional derivatives w.r.t. the source function j. In particular

$$\left. \frac{\delta W[j]}{\delta j(x)} \right|_{j=0} = \langle \phi(x) \rangle \equiv \varphi(x) \tag{2}$$

and

$$\left. \frac{\delta^2 W[j]}{\delta j(x) \delta j(y)} \right|_{j=0} = \langle \phi(x)\phi(y) \rangle - \langle \phi(x) \rangle \langle \phi(y) \rangle \equiv G(x,y) \; . \tag{3}$$

The central object of the FRG is the effective action $\Gamma[\varphi]$ as the Legendre transform of $W[j]$:

$$\Gamma[\varphi] = -W[j] + \int d^4x \; \varphi(x) j(x) \; . \tag{4}$$

It is stationary at the field minimum φ_0 and related to the (grand) canonical potential:

$$\left. \frac{\delta \Gamma[\varphi]}{\delta \varphi} \right|_{\varphi = \varphi_0} = 0; \quad \rightarrow \quad \Omega(T,\mu) = \frac{T}{V} \Gamma[\varphi_0] \; , \tag{5}$$

where T denotes the temperature and μ the chemical potential of the system.

2.2. Wilsonian coarse graining

Wilson's coarse graining [18, 19] starts with a choice of resolution scale k and formally splits the field variable $\phi(x)$ into low- and high-frequency modes:

$$\phi(x) = \phi_{q\leq k}(x) + \phi_{q>k}(x) \ . \tag{6}$$

This allows to rewrite the partition function Z in the following way:

$$Z[j] = \int [\mathcal{D}\phi]_{q\leq k} \underbrace{\int [\mathcal{D}\phi]_{q>k} \ e^{-S[\phi]+\int d^4x \ \phi(x)j(x)}}_{=Z_k[j]} \ , \tag{7}$$

thus introducing a scale-dependent partition function $Z_k[j]$ which becomes the full partition function in the infra-red limit:

$$\lim_{k\to 0} Z_k[j] = Z[j] \ . \tag{8}$$

To render Z ultra-violet and infra-red finite a regulator function $R_k(q)$ is introduced (whose specific form is irrelevant) with the boundary conditions

$$\lim_{k\to 0} R_k(q) = 0 \quad \lim_{k\to\Lambda} R_k(q) = \infty \ , \tag{9}$$

where Λ denotes an ultra-violet cut-off scale. The regulator function adds an additional term $\Delta S_k[\phi]$ to the action such that

$$Z_k[j] = \int [\mathcal{D}\phi] \ e^{-S[\phi]-\Delta S_k[\phi]+\int d^4x \ \phi(x)j(x)} \tag{10}$$

with

$$\Delta S_k[\phi] = \frac{1}{2}\int \frac{d^4q}{(2\pi)^4} \ \phi(-q)R_k(q)\phi(q) \tag{11}$$

formally acting as a k-dependent mass term. For the scale-dependent effective action $\Gamma_k[\varphi]$ this implies

$$\Gamma_k[\varphi] = -\ln Z_k[j] + \int d^4x \ \varphi(x)j(x) - \Delta S_k[\varphi] \ , \tag{12}$$

which interpolates between $k = \Lambda$ where no fluctuations are considered (classical action) and the full quantum action at $k = 0$:

$$\lim_{k\to\Lambda} \Gamma_k[\varphi] = S[\varphi]; \quad \lim_{k\to 0} \Gamma_k[\varphi] = \Gamma[\varphi] \ . \tag{13}$$

2.3. Flow equations

The scale-dependence of the effective action Γ_k is governed by an exact flow equation [20],

$$\partial_k \Gamma_k[\varphi] = \frac{1}{2}\,\mathrm{Tr}\left(\partial_k R_k \left[\Gamma_k^{(2)} + R_k\right]^{-1}\right) , \tag{14}$$

where the trace involves integration of internal momenta as well as summations over internal indices. The flow equation involves the propagator $\Gamma_k^{(2)}$ as a second functional derivative,

$$\Gamma_k^{(2)}(q) = \frac{\delta^2 \Gamma_k[\varphi]}{\delta\varphi(-q)\delta\varphi(q)} , \tag{15}$$

which is graphically represented in Fig. 1 by a one-loop equation for theories involving both bosonic (dashed line) and fermionic (full line) degrees of freedom.

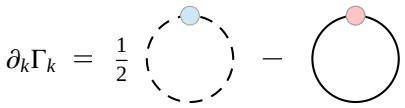

Figure 1: (color online) Diagrammatic representation of the flow equation for the effective action. Dashed (solid) lines represent bosonic (fermionic) propagators and circles represent regulator insertions $\partial_k R_k$.

3. The O(4) model

For illustrative purposes and to introduce the approximations involved in the analytic continuation for real-time spectral functions we start with a simple model system, the O(4) linear-sigma model, involving an iso-triplet of pions and the sigma meson:

$$\varphi = (\varphi_1, \ldots, \varphi_4) = (\sigma, \vec{\pi}) . \tag{16}$$

For the vacuum, results for the sigma and the pion spectral functions have been presented in [21]. The starting point is the effective action of the O(4) model. Even though the exact flow equations can be written down concisely, they are functional equations that are difficult to solve. For practical applications one

has to resort to truncations. In a simple possibility, which has proven quite successful in many instances, one is guided by an expansion of Γ_k in the number of space-time derivatives. To lowest order only the potential U of a given Lagrangian becomes scale dependent (local potential approximation (LPA)) and the corresponding O(4)-action reads:

$$\Gamma_k[\varphi] = \int d^4x \left\{ \frac{1}{2}(\partial_\mu \varphi)^2 + U_k(\varphi^2) - c\sigma \right\}; \quad \varphi^2 = \varphi_i \varphi^i = \sigma^2 + \vec{\pi}^2 \, . \tag{17}$$

Using the Wetterich equation, Eq. (14), one easily obtains the following flow equation for the effective potential,

$$\partial_k U_k = I_\sigma + 3I_\pi; \quad I_i = \frac{1}{2}\mathrm{Tr_q}\left(\partial_k R_k(q) \left[\Gamma^{(2)}_{k,i}(q) + R_k(q) \right]^{-1} \right) \, . \tag{18}$$

For a simple choice of the regulator function $R_k(q)$,

$$R_k(q) = (k^2 - \vec{q}^{\,2})\Theta(k^2 - \vec{q}^{\,2}) \, , \tag{19}$$

the loop functions right-hand side of the flow equation takes a simple analytic form,

$$I_i = \frac{k^4}{3\pi^2} \frac{1}{2E_i} \, , \tag{20}$$

with

$$E_\pi = \sqrt{k^2 + 2U'}; \quad E_\sigma = \sqrt{k^2 + 2U' + 4U''\varphi^2}; \quad U' = \frac{\partial U}{\partial \varphi^2} \text{ etc.} \tag{21}$$

In order to solve the flow equation for the effective potential, Eq. (18), the radial field component σ is discretized along a one-dimensional grid in field space while the angular field components are set to their expectation value, $\langle \vec{\pi} \rangle = 0$. In this way the original partial differential equation turns into a set of ordinary differential equations which can be solved numerically [24].

Taking two functional derivatives of the flow equation for Γ_k, Eq. (17), yields the flow equations for the inverse propagators, which are graphically depicted in Fig. 2.[1] These require knowledge of 3- and 4-point vertex functions which

[1] Explicit expressions for the flow equations are given in [21].

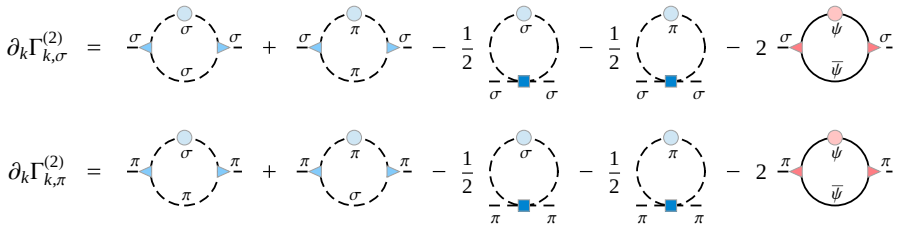

Figure 2: (color online) Diagrammatic representation of the flow equation for the sigma and pion 2-point functions for the quark-meson model. In the case of the O(4) model the quark loop does not appear.

we obtain from the corresponding momentum independent but scale dependent couplings of the effective average action in the LPA. We emphasize that our truncation is thermodynamically consistent in the sense that the static screening masses obtained from the 2-point functions agree with the masses obtained from the curvature of the effective potential, as can be seen from the flow equations which satisfy

$$\partial_k\Gamma^{(2)}_{k,\pi}(p=0) = 2\partial_k U'_k \,, \tag{22}$$

$$\partial_k\Gamma^{(2)}_{k,\sigma}(p=0) = 2\partial_k U'_k + 4\partial_k U''\varphi^2 \,. \tag{23}$$

This also obviates the symmetry-preserving character of the truncation in that it yields the pion as a Nambu-Goldstone boson in the chiral limit ($c=0$).

In order to obtain the sigma and pion spectral functions, we calculate the retarded inverse propagator by analytically continuing the flow equations from imaginary to real time,

$$\Gamma^{(2)R}_{k,j}(\omega) = -\lim_{\epsilon\to 0}\Gamma^{(2)E}_{k,j}(p_0 = i\omega - \epsilon)) \,, \quad j=\pi,\sigma \,, \tag{24}$$

where the real parameter ϵ is kept small but finite in the numerical calculations. The resulting flow equations for the retarded 2-point functions are then solved using the scale-dependent (but momentum independent) 3- and 4-point vertices as well as quasi-particle masses and energies extracted from the LPA result for the scale-dependent effective average action. Moreover, the radial field component σ is set to its expectation value in the infra-red, as determined from the

a/Λ^2	b	c/Λ^3	f_π	$m_\pi^{\rm scr}$	$m_\sigma^{\rm scr}$
-0.30	3.65	0.014	93.0	137.2	425.0
-0.34	3.40	0.002	93.1	16.4	299.8

Table 1: Parameter sets for a UV cutoff $\Lambda = 500$ MeV corresponding to two different pion masses. The physical parameters, f_π and the meson masses, are given in MeV.

global minimum of the effective potential. Finally, the spectral functions are given by

$$\rho_j(\omega) = \frac{1}{\pi} \frac{\mathrm{Im}\,\Gamma_j^{(2)R}(\omega)}{\left(\mathrm{Re}\,\Gamma_j^{(2)R}(\omega)\right)^2 + \left(\mathrm{Im}\,\Gamma_j^{(2)R}(\omega)\right)^2}\,, \quad j = \pi, \sigma\,. \tag{25}$$

3.1. Spectral functions in the vacuum

The following results for the sigma and pion spectral functions were obtained using the parameter sets given in Table 1, where the potential was chosen as $U_{k=\Lambda} = a\phi^2 + b\phi^4$ in the UV.

In Fig. 3 we show the spectral functions for physical pion mass, $m_\pi = 137$ MeV, (left) as well as near the chiral limit $m_\pi = 16$ MeV (right). For the physical mass, the pion spectral function exhibits a sharp peak at 135 MeV, as one would expect, while the sigma spectral function starts at the 2-pion threshold with a sharp increase in the spectral density, followed by a broad maximum at about 312 MeV above this threshold. Although, in the ultra-violet, the sigma meson is sharp it acquires a large decay width during the $k \to 0$ evolution from the decay into two pions.

When approaching the chiral limit, one expects the spectral weight of the pion pole to increase more and more as this pole moves closer to the $\omega = 0$ axis, where it eventually accumulates the full spectral weight. The spectral sum rule implies that all other contributions to the spectral function should decrease with decreasing pion mass. Both trends are seen in Fig. 3 where we have extended the frequency range to include the $\pi^* \to \sigma\pi$ threshold in the pion spectral function.

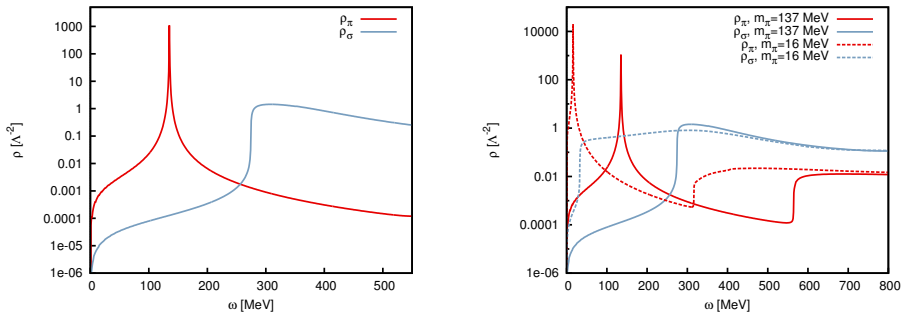

Figure 3: (color online) Pion (ρ_π) and sigma meson (ρ_σ) spectral functions from [21] for two different parameter sets.

4. In-medium spectral functions

We now apply the method, presented above, to strong-interaction matter within the quark-meson model for finite temperature and density [17]. The quark-meson model serves as a low-energy effective model for QCD with $N_\mathrm{f} = 2$ light quark flavors, which shares chiral symmetry and its breaking pattern. The scale-dependent effective average action (in the LPA) reads as follows:

$$\Gamma_k[\bar{\psi},\psi,\varphi] = \int d^4x \Big\{ \bar{\psi}\left(\partial\!\!\!/ + h(\sigma + i\vec{\tau}\cdot\vec{\pi}\gamma_5) - \mu\gamma_0\right)\psi + \frac{1}{2}(\partial_\mu\varphi)^2 + U_k(\varphi^2) - c\sigma \Big\} \,. \tag{26}$$

Using the Wetterich equation, Eq. (14), with optimized regulator functions for bosonic and fermionic fields, cf. Eq. (19), the flow equation for the effective potential becomes

$$\partial_k U_k = I_\sigma + 3I_\pi - N_\mathrm{c} N_\mathrm{f} I_\psi, \tag{27}$$

with the loop functions I_i as defined in Eq. (18). As in the case of the O(N) model, the flow equation for the effective potential is solved using the grid method.

The flow equations for the two-point functions are obtained by taking two functional derivatives of Eq. (26) and are represented diagrammatically in Fig. 2. Therein, the quark-meson 3-point vertices are taken to be momentum and scale-independent, $\Gamma^{(2,1)}_{\bar{\psi}\psi\sigma} = h$ and $\Gamma^{(2,1)}_{\bar{\psi}\psi\vec{\pi}} = ih\gamma^5\vec{\tau}$, while the mesonic

m_Λ/Λ	λ_Λ	c/Λ^3	h	f_π	$m_\pi^{\rm scr}$	$m_\sigma^{\rm scr}$	$m_q^{\rm scr}$
0.794	2.00	0.00175	3.2	93.5	138	509	299

Table 2: Parameter set for the quark-meson model with $\Lambda = 1000$ MeV. The pion decay constant as well as the particle masses are given in MeV.

vertices are scale-dependent and given by appropriate derivatives of the effective potential, as in the case of the O(4) model.

In order to obtain the flow equations for the retarded two-point functions, we have to perform an analytic continuation from imaginary to real frequencies. Since we are now working at finite temperature, this analytic continuation is not as straightforward as in the vacuum. However, it can be shown that the following two-step procedure obeys the correct (Baym-Mermin) boundary conditions and yields the proper retarded propagators [22, 23]. Once the sum over the Matsubara frequencies in the flow equations are performed, we first treat the external energy as an imaginary and discrete quantity, $p_0 = i\,2\pi nT$, and exploit the periodicity of the bosonic and fermionic occupation numbers which appear in the flow equations:

$$n_{B,F}(E + ip_0) \to n_{B,F}(E)\ . \tag{28}$$

For explicit expressions of the flow equations we refer to [17]. In a second step, we replace the discrete imaginary external energy by a continuous real energy in order to obtain the retarded 2-point functions, cf. Eq. (24).

As described for the O(4) model above, the flow equations for the real and imaginary parts of the retarded 2-point functions are then solved at the global minimum of the effective potential in the IR. Further details on our numerical implementation are given in [17].

4.1. Results

The results for the quark-meson model were obtained using the parameter set given in Tab. 2, with the UV potential chosen as

$$U_\Lambda(\phi^2) = \tfrac{1}{2}m_\Lambda^2\phi^2 + \tfrac{1}{4}\lambda_\Lambda(\phi^2)^2\ . \tag{29}$$

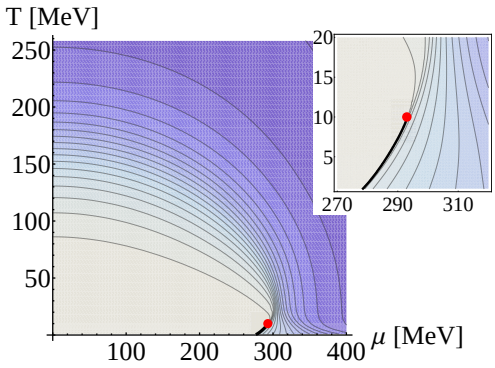

Figure 4: (color online) The phase diagram of the quark-meson model from [17], as obtained by using the parameter set in Tab. 2, is illustrated by a contour plot of the magnitude of the chiral order parameter, $\sigma_0 \equiv f_\pi$, vs. quark chemical potential μ and temperature T. The order parameter decreases towards higher μ and T, as indicated by a darker color.

We first briefly discuss the resulting phase diagram as it serves as input for the calculation of the spectral functions. It is shown in Fig. 4 and displays the typical shape [24] found in quark-meson model calculations beyond the mean-field approximation with a critical endpoint at $\mu = 293\,\mathrm{MeV}$ and $T = 10\,\mathrm{MeV}$ for this parameter set.[2] In addition, it is also instructive to consider the temperature- and chemical potential-dependence of the meson screening masses as they will be used to identify thresholds in the spectral functions, cf. Fig. 5.

We now turn to the discussion of results for the sigma and pion spectral functions, $\rho_\sigma(\omega)$ and $\rho_\pi(\omega)$. They are displayed in Fig. 6 as a function of external energy ω at different values of T and μ . The inserted numbers refer to different processes contributing to the spectral functions via the corresponding diagrams shown in Fig. 2. The sigma spectral function is affected by the processes $\sigma^* \to \sigma\sigma$ (1), $\sigma^* \to \pi\pi$ (2) and $\sigma^* \to \bar{\psi}\psi$ (3), where primes denote off-shell correlations with energy ω. The relevant processes for the pion spectral

[2]The low value for the chiral endpoint should not be of concern, since its location strongly depends on parameter choices and effects from Polyakov-loop extensions of the model.

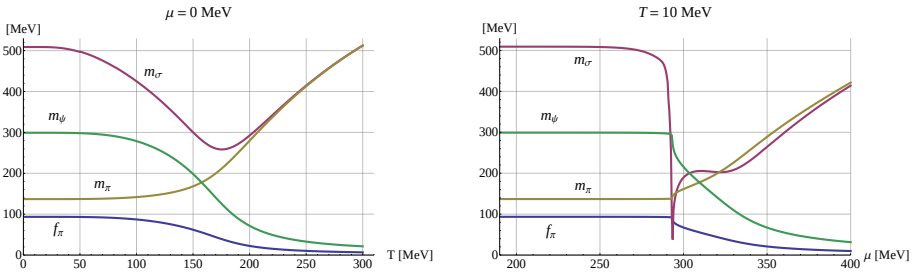

Figure 5: (color online) The meson screening masses, the quark mass and the chiral order parameter, $\sigma_0 \equiv f_\pi$, are shown vs. temperature T at $\mu = 0\,\mathrm{MeV}$ (left panel), and vs. quark chemical potential μ at $T = 10\,\mathrm{MeV}$ (right panel), taken from [17].

function are $\pi^* \to \sigma\pi$ (4), $\pi^*\pi \to \sigma$ (5) and $\pi^* \to \bar{\psi}\psi$ (6). In our truncation with momentum-independent vertices the mesonic tadpole diagrams only give rise to ω-independent contributions to the spectral functions.

At $T = 10\,\mathrm{MeV}$ and $\mu = 0\,\mathrm{MeV}$ the spectral functions closely resemble those in the vacuum, observed in the case of the O(4) model, with the addition of the quark-antiquark decay channel. When going to higher temperatures, the thermal scattering process $\pi^*\pi \to \sigma$, affects to the pion spectral function for $\omega \leq m_\sigma - m_\pi$. Another effect induced by the temperature dependence of the meson and quark masses is the emergence of a stable sigma meson at temperatures close to the crossover temperature, where neither the decay into two pions nor that into two quarks are energetically possible. At $T = 150\,\mathrm{MeV}$ we therefore observe a pronounced peak in the sigma spectral function at $\omega \approx 280\,\mathrm{MeV}$. When increasing the temperature further, the quarks become the lightest degrees of freedom in the system, providing decay channels for both the pion and the sigma meson. At very high temperatures the spectral functions become degenerate, as to be expected from the progressing restoration of chiral symmetry.

The right column of Fig. 6 shows the sigma and pion spectral functions at a fixed temperature of $T = 10\,\mathrm{MeV}$ and different values of the quark chemical potential. Up to chemical potentials of around 200 MeV the spectral functions remain essentially unchanged since the ground state is unaffected by the chem-

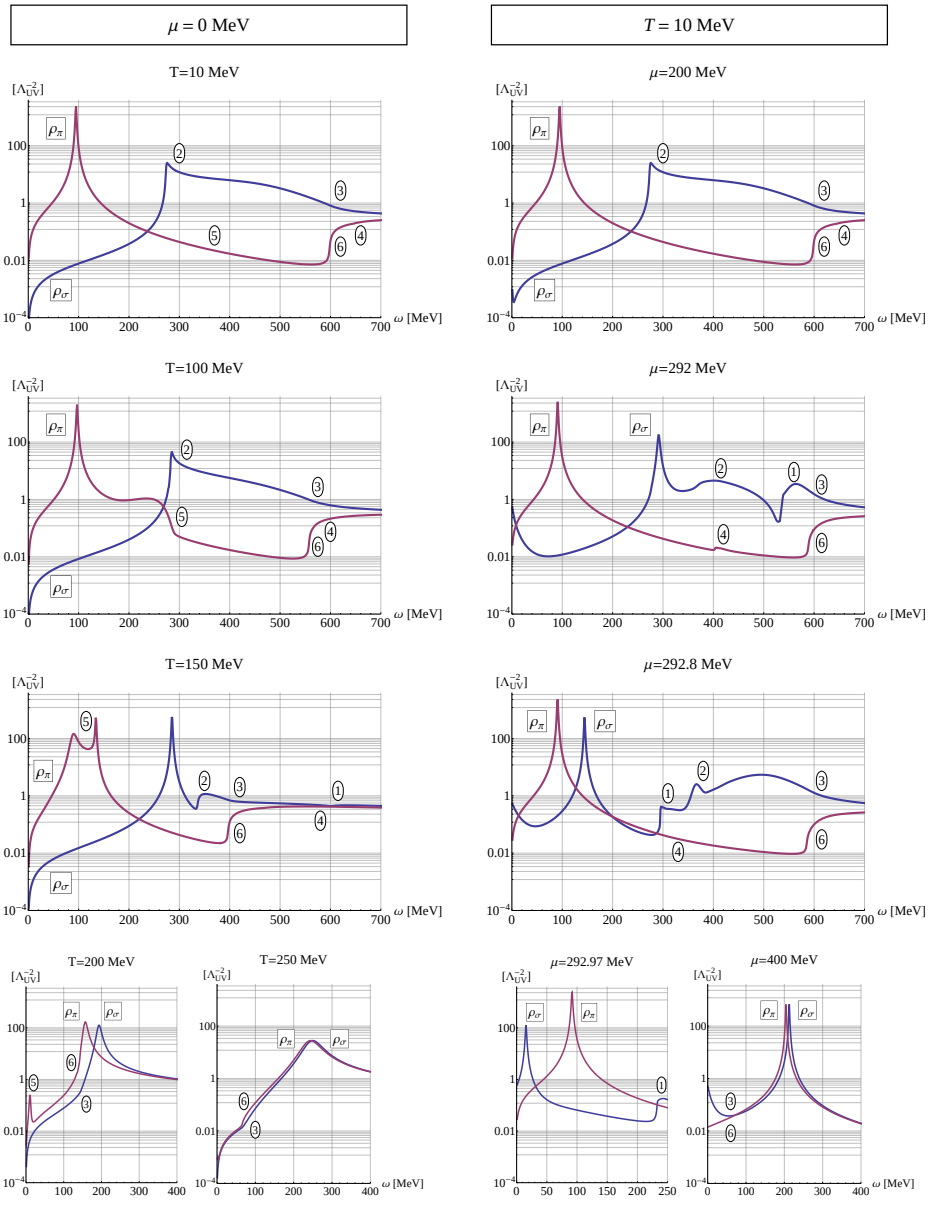

Figure 6: (color online) Sigma and pion spectral function from [17] are shown versus external energy ω at $\mu = 0\,\mathrm{MeV}$ but different T (left column) and at $T = 10\,\mathrm{MeV}$ but different μ (right column). Inserted numbers refer to the different processes affecting the spectral functions at corresponding energies. 1: $\sigma^* \to \sigma\sigma$, 2: $\sigma^* \to \pi\pi$, 3: $\sigma^* \to \bar{\psi}\psi$, 4: $\pi^* \to \sigma\pi$, 5: $\pi^*\pi \to \sigma$, 6: $\pi^* \to \bar{\psi}\psi$. See text for details.

ical potential below the phase transition (Silver Blaze property, [25]). When approaching the critical endpoint, however, especially the sigma spectral function undergoes significant changes. At $\mu = 292\,\mathrm{MeV}$, i.e. only about 1 MeV from the critical endpoint, the sigma screening mass has already dropped to about half of its vacuum value, leading to a minimal energy for the $\sigma^* \to \sigma\sigma$ decay of $\omega \geq 2\,m_\sigma \approx 540\,\mathrm{MeV}$. In addition, a pronounced sigma peak starts to develop at $\omega \approx 290\,\mathrm{MeV}$, indicating the formation of a stable dynamical sigma meson. Even closer to the CEP, at $\mu = 292.8\,\mathrm{MeV}$, the threshold for the two-sigma decay has decreased to $\omega \approx 290\,\mathrm{MeV}$ and thus occurs already at smaller energies than the $\sigma^* \to \pi\pi$ process. At $\mu = 292.97\,\mathrm{MeV}$, the sigma meson has become almost massless, as expected near a second order phase transition. When increasing the chemical potential further, the sigma and pion spectral functions become degenerate, similar to the case of high temperatures.

5. Summary and Outlook

In this contribution we have presented a tractable scheme for obtaining hadronic spectral functions at finite temperature and density within the FRG approach. The method is based on an analytic continuation from imaginary to real frequencies on the level of the flow equations for the pertinent two-point functions. It is thermodynamically consistent and symmetry preserving. As a consequence, phase transitions and critical behavior can be properly handled.

We have demonstrated the feasibility of the method by applying it to the O(4) linear-sigma model in the vacuum and to the quark-meson model at finite temperature and density. Many additional in-medium scattering processes result in a rather complicated structure of the spectral functions, clearly exhibiting the critical behavior in the vicinity of chiral phase transitions. As chiral symmetry gets restored at high temperature and density the spectral function of the pion and the sigma meson, as its chiral partner, become degenerate and thus lead to parity doubling.

Apart from extensions to other spectral functions, such as those of the ρ

and a_1 meson, which are of relevance for electromagnetic probes in heavy-ion collisions, there is also the exciting possibility to compute transport coefficients in the entire (T, μ)-plane of the phase diagram.

6. Acknowledgements

We dedicate this article to Gerry Brown, an inspiring physicist and a great human being. We would like to thank K. Kamikado for collaboration. This work was supported by the Helmholtz International Center for FAIR within the LOEWE initiative of the state of Hesse. R.-A. T. is furthermore supported by the Helmholtz Research School for Quark Matter Studies, H-QM, and N. S. is supported by Grant No. ERC-AdG-290623.

References

[1] G. Brown, M. Rho, Scaling effective Lagrangians in a dense medium, Phys.Rev.Lett. 66 (1991) 2720–2723. doi:10.1103/PhysRevLett.66.2720.

[2] G. Brown, M. Rho, Double decimation and sliding vacua in the nuclear many body system, Phys.Rept. 396 (2004) 1–39. arXiv:nucl-th/0305089, doi:10.1016/j.physrep.2004.02.002.

[3] J. Berges, N. Tetradis, C. Wetterich, Nonperturbative renormalization flow in quantum field theory and statistical physics, Phys.Rept. 363 (2002) 223–386. arXiv:hep-ph/0005122.

[4] J. Polonyi, Lectures on the functional renormalization group method, Central Eur.J.Phys. 1 (2003) 1–71. arXiv:hep-th/0110026, doi:10.2478/BF02475552.

[5] J. M. Pawlowski, Aspects of the functional renormalisation group, Annals Phys. 322 (2007) 2831–2915. arXiv:hep-th/0512261, doi:10.1016/j.aop.2007.01.007.

[6] B.-J. Schaefer, J. Wambach, Renormalization group approach towards the qcd phase diagram, Phys.Part.Nucl. 39 (2008) 1025–1032. arXiv:hep-ph/0611191, doi:10.1134/S1063779608070083.

[7] P. Kopietz, L. Bartosch, F. Schutz, Introduction to the functional renormalization group, Lect.Notes Phys. 798 (2010) 1–380. doi:10.1007/978-3-642-05094-7.

[8] J. Braun, Fermion interactions and universal behavior in strongly interacting theories, J.Phys. G39 (2012) 033001. arXiv:1108.4449, doi:10.1088/0954-3899/39/3/033001.

[9] H. Gies, Introduction to the functional rg and applications to gauge theories, Lect. Notes Phys. 852 (2012) 287–348. arXiv:hep-ph/0611146.

[10] H. J. Vidberg, J. W. Serene, Solving the Eliashberg equations by means of N-point Padé approximants, Journal of Low Temperature Physics 29 (1977) 179–192. doi:10.1007/BF00655090.

[11] M. Jarrell, J. Gubernatis, Bayesian inference and the analytic continuation of imaginary-time quantum monte carlo data, Physics Reports 269 (3) (1996) 133 – 195. doi:10.1016/0370-1573(95)00074-7.

[12] M. Asakawa, T. Hatsuda, Y. Nakahara, Maximum entropy analysis of the spectral functions in lattice QCD, Prog.Part.Nucl.Phys. 46 (2001) 459–508. arXiv:hep-lat/0011040, doi:10.1016/S0146-6410(01)00150-8.

[13] D. Dudal, O. Oliveira, P. J. Silva, Källén-Lehmann spectroscopy for (un)physical degrees of freedom. arXiv:1310.4069.

[14] N. Strodthoff, B.-J. Schaefer, L. von Smekal, Quark-meson-diquark model for two-color QCD, Phys.Rev. D85 (2012) 074007. arXiv:1112.5401, doi:10.1103/PhysRevD.85.074007.

[15] K. Kamikado, N. Strodthoff, L. von Smekal, J. Wambach, Fluctuations in the quark-meson model for QCD with isospin chemical potential, Phys.Lett.

B718 (2013) 1044–1053. arXiv:1207.0400, doi:10.1016/j.physletb.2012.11.055.

[16] S. Floerchinger, Analytic Continuation of Functional Renormalization Group Equations, JHEP 1205 (2012) 021. arXiv:1112.4374, doi:10.1007/JHEP05(2012)021.

[17] R.-A. Tripolt, N. Strodthoff, L. von Smekal, J. Wambach, Spectral Functions for the Quark-Meson Model Phase Diagram from the Functional Renormalization Group, Phys.Rev. D89 (2014) 034010. arXiv:1311.0630, doi:10.1103/PhysRevD.89.034010.

[18] K. G. Wilson, Renormalization group and critical phenomena. ii. phase-space cell analysis of critical behavior, Phys. Rev. B 4 (1971) 3184–3205. doi:10.1103/PhysRevB.4.3184.

[19] K. Wilson, J. B. Kogut, The Renormalization group and the epsilon expansion, Phys.Rept. 12 (1974) 75–200. doi:10.1016/0370-1573(74)90023-4.

[20] C. Wetterich, Exact evolution equation for the effective potential, Phys. Lett. B301 (1993) 90–94. doi:10.1016/0370-2693(93)90726-X.

[21] K. Kamikado, N. Strodthoff, L. von Smekal, J. Wambach, Real-Time Correlation Functions in the O(N) Model from the Functional Renormalization Group, Eur.Phys.J. C74 (2014) 2806. arXiv:1302.6199, doi:10.1140/epjc/s10052-014-2806-6.

[22] G. Baym, N. D. Mermin, Determination of thermodynamic green's functions, J. Math. Phys. 2 (1961) 232. doi:http://dx.doi.org/10.1063/1.1703704.

[23] N. Landsman, C. van Weert, Real and Imaginary Time Field Theory at Finite Temperature and Density, Phys.Rept. 145 (1987) 141. doi:10.1016/0370-1573(87)90121-9.

[24] B.-J. Schaefer, J. Wambach, The phase diagram of the quark meson model, Nucl. Phys. A757 (2005) 479–492. arXiv:nucl-th/0403039, doi:10.1016/j.nuclphysa.2005.04.012.

[25] T. D. Cohen, Functional integrals for QCD at nonzero chemical potential and zero density, Phys.Rev.Lett. 91 (2003) 222001. arXiv:hep-ph/0307089, doi:10.1103/PhysRevLett.91.222001.